Materials Today Physics 24 (2022) 100658

Contents lists available at ScienceDirect

Materials Today Physics

journal homepage: https://www.journals.elsevier.com/materials-today-physics

Electronic and phononic origins of $BaSO_4$ as an ultra-efficient radiative cooling paint pigment

Z. Tong [a, b, c, 1], J. Peoples [a, 1], X. Li [a, d], X. Yang [a, e], H. Bao [b, *], X. Ruan [a, **]

[a] School of Mechanical Engineering and the Birck Nanotechnology Center, Purdue University, West Lafayette, IN, 47907-2088, USA
[b] University of Michigan-Shanghai Jiao Tong University Joint Institute, Shanghai Jiao Tong University, Shanghai, 200240, China
[c] Shenzhen JL Computational Science and Applied Research Institute, Shenzhen, 518131, China
[d] Device Research Laboratory, Department of Mechanical Engineering, Massachusetts Institute of Technology, Massachusetts, 02139, USA
[e] Institute for Advanced Study, Shenzhen University, Nanhai Avenue 3688, Shenzhen, 518060, China

ARTICLE INFO

Article history:
Received 23 January 2022
Received in revised form
6 March 2022
Accepted 8 March 2022
Available online 18 March 2022

Keywords:
Radiative cooling
First-principles calculation
Monte Carlo simulation
Nanocomposites

ABSTRACT

Radiative cooling has recently revived because of its significant potential for saving energy and combating climate change. Several ultra-efficient particle-matrix cooling nanocomposites such as $BaSO_4$-acrylic paints have been demonstrated via trial-and-error approaches, but the atomistic characteristics of their pigments remain elusive. In this work, we use first-principles calculations to predict the full-spectrum optical constants of $BaSO_4$, and successfully explain the ultra-high reflectance in the solar spectrum (0.28–2.5 μm) and simultaneously high normal emittance in the sky window (8–13 μm) observed in previous experiments. Efficient radiative cooling pigments require high refractive index n and low extinction coefficient κ in the solar spectrum. However, our results show that they cannot be tuned independently, but are both tied to the electronic band gap. Eliminating κ would require a high band gap, which would yield low n, creating a dilemma to address for radiative cooling. By systematic comparison, we show that $BaSO_4$ outperforms the commonly used α-quartz (α-SiO_2), and we identify two pertinent characters of $BaSO_4$: i) Although the band gap of $BaSO_4$ is high enough to eliminate solar absorption, it is also moderate enough to enable reasonably high refractive index for strong scattering, and ii) $BaSO_4$ has complex crystal structure and appropriate bond strength that yield a high number of infrared-active zone-center optical phonon modes in the Reststrahlen bands, and these modes show strong four-phonon scattering which is a previously unknown mechanism that contributes to the high emissivity in the sky window. Our first-principles approach and physical insights pave the way for further search of efficient radiative cooling materials.

1. Introduction

Radiative cooling is a passive cooling technology that has received tremendous attention recently, due to its promise of not only saving energy but also combating climate change, since it sends off the heat to space rather than leaves heat on the earth. Many materials have been explored for cooling of buildings [1], solar cells [2], power plants [3], harvesting dew water [4], and desalination [5], etc. Ideal materials for radiative cooling should have high reflectance (low emissivity) in the solar spectrum and high emissivity in the sky window region [6–9]. As such, designing radiative cooling materials or devices with tailored spectral properties has attracted significant research interest. Since 1960s, radiative cooling has been pursued [10–13]. In particular, a TiO_2 paint-aluminum substrate dual-layer showed full daytime below-ambient cooling during a winter day [11], but the solar reflectance primarily comes from the metal substrate instead of the paint itself, hence substrate-independent cooling was not demonstrated. Moreover, fabricating polymer-based metamaterial or composites have been extensive explored such as coating the reflective metal with thin layer polymer (e.g. polyvinyl fluoride [10], polyphenylenoxid [14], or polymethylpentene [15]) and mixing infrared transmitting polymers with nanoparticles (e.g. SiC or SiO_2 [16] and TiO_2 [17]). In addition, engineering-based structure geometric technologies have also been employed for designing radiative

* Corresponding author.
** Corresponding author.
E-mail addresses: hua.bao@sjtu.edu.cn (H. Bao), ruan@purdue.edu (X. Ruan).
[1] These authors contribute equally to this work.

https://doi.org/10.1016/j.mtphys.2022.100658
2542-5293/

devices, for instance, manipulating the zenith angle of the radiative cooling surface [18], adopting inverted mirror cone [19], infrared reflective trough for concentrated radiative cooling [20], etc. In the last decade, the interest in radiative cooling was renewed [16]. Full daytime radiative cooling was achieved in nanophotonic multilayers [21], and subsequently in other non-paint approaches including polymer-metal dual layer [22], silica nanocomposite-metal dual layer [23], silica-metal dual layer [24], metamaterial [25], visibly transparent radiative cooler [26], nanoparticle mixture coating [27], silica-coated porous anodic aluminum oxide [28], and delignified wood [29]. Meanwhile, the cooling paint approach has occurred to predict full daytime radiative cooling theoretically [30–32], and full daytime cooling has been experimentally demonstrated in porous polymers [33] and commercial-like $CaCO_3$-acrylic and $BaSO_4$-acrylic paints [34–36], providing a viable radiative cooling solution. The paints approach has used large electronic band gaps in $CaCO_3$ and $BaSO_4$ to eliminate the solar absorption and used 60 vol% concentration and hierarchical particle size to maximize scattering of the solar spectrum. In particular, the $BaSO_4$-acrylic paint shows an ultra-high solar reflectance of 98.1% and sky-window emissivity of 0.95, which enable net cooling power of $>$ 100 W/m^2 under direct sunlight [34,36].

However, the pursuit of these efficient particle-matrix paints has been via trial-and-error process. The atomistic structural metrics that lead to ultra-efficient radiative cooling paints such as the $BaSO_4$-acrylic paint [34,36] are lacking. Overall, to achieve highest possible solar reflectance, one prefers high reflective index n and zero extinction coefficient κ in the solar spectrum. It is known that the conventional pigment TiO_2 offers high refractive index which provides strong scattering, but it absorbs UV light due to its insufficient band gap. Therefore, a larger band gap of the filler is needed to eliminate solar absorption, such as SiO_2, $CaCO_3$, and $BaSO_4$. However, their refractive index is lower than that of TiO_2 and the scattering will be weaker, hence is it really the band gap larger, the better? There appears a dilemma between increasing the reflective index and eliminating the extinction coefficient. It is also known that resonant vibrational modes are needed to enable high emissivity in the sky window. However, questions are open on how their linewidth features and mechanisms may affect the cooling performance. Nevertheless, the optical constants of most solids including $BaSO_4$ are neither known experimentally or theoretically in the literature, but crucial to understand their radiative cooling capability. Answering these questions call for predictive approaches and physical insights, to understand their performance and facilitate the design of better radiative cooling paints in the future.

In this work, we illustrate the effectiveness of combining first-principles calculations and Monte Carlo simulations to predict and understand the high performance of radiative cooling materials. We uncover the optical constants of $BaSO_4$ and quantitatively explain why it is a better radiative cooling material than SiO_2 that is the state-of-the-art [6,9,16]. The dielectric function of $BaSO_4$ in both solar spectrum and mid-infrared (mid-IR) region is determined from first-principles, where the Bethe-Salpeter equation [37,38] (BSE) and anharmonic lattice dynamics are employed for accurately describing the photon-electron interactions [39–42] and photon-lattice absorptions [43–46], respectively. The dielectric function is then used in Monte Carlo simulations to obtain the transmittance, reflectance, and emittance (or absorptance) of nanoparticle composites [30,32,47–50]. Our analysis show that since generally the refractive index is negatively correlated with the electronic band gap, we cannot tune the refractive index and extinction coefficient independently, but they are both tied to the band gap. Therefore, the band gap is the more fundamental parameter we should consider to weigh the dilemma of increasing n and eliminating κ. In the case of $BaSO_4$, although its electronic band gap is known to be wide enough to eliminate solar absorption [34,36], here we point out that it is also moderate enough at the same time to enable reasonably high refractive index for strong scattering. Meanwhile, its complex crystal structure and appropriate bond strength give a high number of infrared-active zone-center optical phonon modes in the Reststrahlen bands, and these modes show strong four-phonon scattering, which represents a previously unknown mechanism that contributes to the high emissivity in the sky window. Our approach and the identified atomistic metrics provide effective tools and insights to design efficient radiative cooling paints in the future.

2. Methods and simulation details

We have implemented a first-principles approach to obtain the dielectric function. In the solar spectrum, photons are absorbed through electronic transition. By summing all the possible vertical transitions across the band gap, the imaginary part $\epsilon''(\omega)$ shown in Eq. (S1) of the dielectric function can be determined based on the Fermi's golden rule [51,52]. The real part $\epsilon'(\omega)$ of the dielectric function can be further obtained from $\epsilon''(\omega)$ through Kramers-Krönig transformation [51].

$$\epsilon'(\omega) = 1 + \frac{2}{\pi} P \int_0^\infty \frac{\epsilon''(\omega')\omega'}{\omega'^2 - \omega^2} d\omega', \tag{1}$$

where P is the principal value of the integral.

In the mid-IR band, the dielectric function is described by the Lorentz oscillator model [53,54].

$$\frac{\epsilon(\omega)}{\epsilon_\infty} = \prod_j \frac{\omega_{j,\mathrm{LO}}^2 - \omega^2 + \mathrm{i}\gamma_{j,\mathrm{LO}}\omega}{\omega_{j,\mathrm{TO}}^2 - \omega^2 + \mathrm{i}\gamma_{j,\mathrm{TO}}\omega}, \tag{2}$$

where ϵ_∞ is the high frequency dielectric constant, ω_j is the resonance frequency, j goes over all the IR-active modes, and γ_j is the phonon damping factor of the j-th resonance phonon mode. LO and TO denote the longitudinal and transverse optical phonon modes, respectively. By employing anharmonic lattice dynamics method, γ_j (or scattering rate τ_j^{-1}) can be calculated using the harmonic and anharmonic interatomic force constants (IFCs) from first-principles calculations [43–46]. We note here that beyond the phonon damping factor from the standard three-phonon scattering (3ph), we have found that four-phonon scattering (4ph) is significant, hence our $\gamma_j = \gamma_j^{3\mathrm{ph}} + \gamma_j^{4\mathrm{ph}}$, where $\gamma_j^{3\mathrm{ph}}$ and $\gamma_j^{4\mathrm{ph}}$ are the phonon damping originating from 3ph to 4ph scatterings, respectively.

All the *ab initio* calculations are performed based on density functional theory (DFT) by employing the projector-augmented-wave (PAW) method [55] as implemented in the Vienna ab initio simulation package (VASP) [56]. Since the ground state DFT is known to underpredict the band gap [41,57], here the self-consistent quasiparticle GW (sc-QPGW) method [41] is used for more accurate prediction. The second-order IFCs (harmonic) are extracted from density functional perturbation theory (DFPT) using Phonopy package [58] while the third-order IFCs are computed from the finite difference method using THIRDORDER. PY package [59]. The 3ph scattering damping is calculated using the ShengBTE package [59], while the 4ph scattering damping is computed with an in-house code [45,60–63]. Finally, the emittance, reflectance, and transmittance of α-SiO_2- and $BaSO_4$-based nanocomposites are calculated using our utilized [32] open-source Monte Carlo code [49] which simulates photon transport in turbid medium. More

theory and computational details are given in the Supplemental Material [64]. Importantly, in order to validate our calculations, we first apply our methodology to α-SiO_2 which is a benchmark radiative cooling material with sufficient existing experimental data.

3. Results and discussions

3.1. Electronic and phononic band structure

The calculated band structure and harmonic phonon dispersion for α-SiO_2 and $BaSO_4$ are shown in Fig. 1, and their atomic structures and optimized lattice constants are provided in Supplemental Material, Fig. S1 and Table S1. The calculated band gaps are 8.73 eV for α-SiO_2 (measured value is 8.90 eV [57]) and 7.27 eV for $BaSO_4$ (experimental value is 7.60 eV [65]), which are also depicted in their band structures as shown in Fig. 1(a)-1(b), respectively. The prediction-measurement agreement is excellent, laying the foundation of the following dielectric function calculations. Here, we observe that the band gaps of both α-SiO_2 and $BaSO_4$ are higher than the energy of photons located in the solar spectrum with a range of 0.49 ~ 4.13 eV (0.28−2.5 μm). As such, it is not surprising there is no photon absorption in the solar spectrum for both α-SiO_2 and $BaSO_4$.

The harmonic phonon dispersions along high symmetry paths in the first Brillouin zone are shown in Fig. 1(c)-1(d) for α-SiO_2 and $BaSO_4$, respectively. Previously reported phonon frequencies [66] of α-SiO_2 are also presented in Fig. 1(c), with which our predictions agree. We note that the phonon renormalization at finite temperature is not considered here, since at room temperature it only needs to be considered for strongly anharmonic materials [44], which is not the case for the materials used in this work. A key insight is that we observed more zone-center ($\mathbf{q} = 0$) optical modes in $BaSO_4$ than in α-SiO_2 in the sky window region (8−13 μm) as depicted with blue shaded regions in Fig. 1(c)-1(d). Moreover, according to space-group theory analysis [67,68], the irreducible representations of zone-center optical phonon modes are denoted with $4A_1+4A_2+8E$ for α-SiO_2 and $11A_g+7B_{1g}+11B_{2g}+7B_{3g}+7A_u+10B_{1u}+6B_{2u}+10B_{3u}$ for $BaSO_4$, in which the IR-active modes are $4A_2+8E$ for α-SiO_2 while $10B_{1u}+6B_{2u}+10B_{3u}$ for $BaSO_4$, verifying that $BaSO_4$ owns more IR-active phonon modes than that of α-SiO_2.

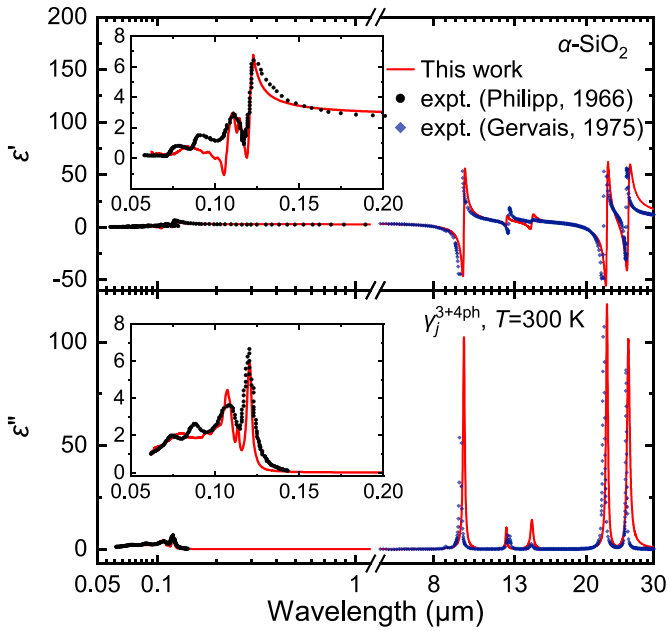

Fig. 2. Dielectric function of α-SiO_2 in the wavelength range of 0.05−30 μm at room temperature. The experimental data in the ultraviolet−visible band are taken from Ref. [69] (black circle dot) while those in the mid-IR region are from Ref. [70] (navy diamond dot).

3.2. Optical constants from first-principles

The dielectric function is calculated for α-SiO_2 and $BaSO_4$, and the results of α-SiO_2 are shown in Fig. 2 to validate against experimental data. As seen, good agreements of the dielectric function between our calculations and reported data in both solar spectrum [69] and mid-IR region [70] are achieved, demonstrating the

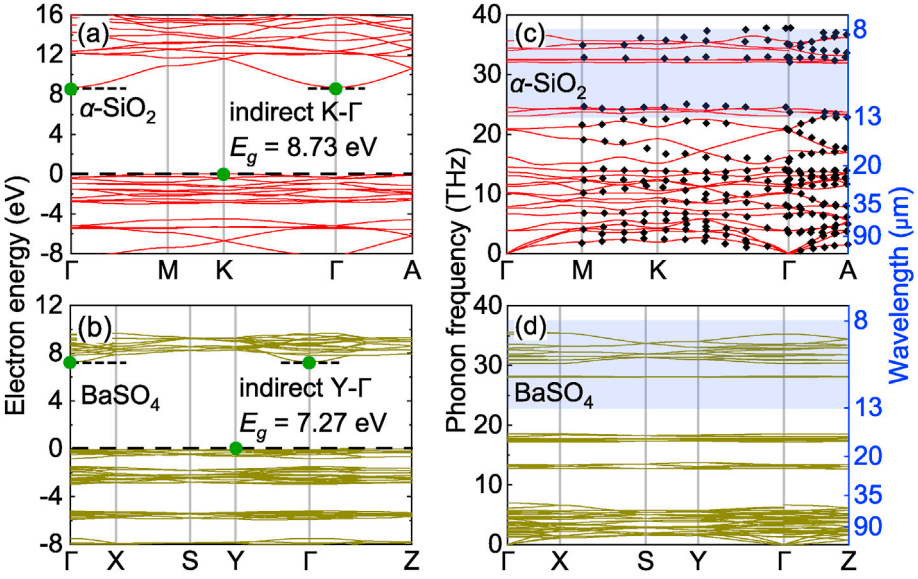

Fig. 1. Calculated band structure for α-SiO_2 in (a) and $BaSO_4$ in (b), and harmonic phonon dispersion in (c) and (d) from first-principles, respectively. Experimentally measured [66] phonon frequency (black diamond) of α-SiO_2 is also presented in (c) for comparison. Indirect band gaps are denoted using green dot at high symmetry point in the first Brillouin zone with K-Γ in (a) and Y-Γ in (b) for α-SiO_2 and $BaSO_4$, respectively. The wavelength corresponding to phonon frequency is presented using blue right-*y* axis, and the sky window ranging in 8−13 μm is depicted by shaded region with blue color in (c) and (d), for α-SiO_2 and $BaSO_4$, respectively.

accuracy of our predictions. The *ab initio* identified IR-active phonon modes and their corresponding values of phonon frequency and damping are provided in Supplemental Material, Table S2.

The real and imaginary parts of the complex refractive index, n and κ, can be obtained through $\epsilon = (n + i\kappa)^2$, and the calculated results for α-SiO_2 and $BaSO_4$ are shown in Fig. 3(a). Our predictions on α-SiO_2 in general agree well with those reported experimental data [70,71]. Notably, the n value of $BaSO_4$ is larger than that of α-SiO_2 in the solar spectrum, which would favor stronger solar scattering and reflectance in $BaSO_4$. We identify that it is because in semiconductors the refractive index is negatively correlated to the band gap [72]. Meanwhile, both materials' band gaps are large enough to result in a zero predicted κ in the solar spectrum. In comparison, experiments show a small and negligible κ which is probably due to impurities or defects. In addition, TiO_2 has much higher refractive index than $BaSO_4$, which benefits more scattering and enables a lower volume concentration of particles than $BaSO_4$. However, the performance of TiO_2 is limited by solar absorption in the ultraviolet band due to the moderate 3.2 eV electron band gap. Theoretical studies have indicated that the solar reflectance of TiO_2-acrylic paint is unlikely to exceed 92% [32]. Therefore, TiO_2-based particle paint layer was generally developed for partial daytime subambient cooling except for the noon hours. ZnO has a similar band gap with TiO_2 hence share similar advantages and disadvantages. On the other hand, $BaSO_4$ possesses a much larger electron band gap and will eliminate the UV absorption. Whereas, due to $BaSO_4$'s lower refractive index the volume concentration of the particles must be much larger to achieve an adequate scattering coefficient which contributes to the high solar reflectance. Furthermore, $BaSO_4$ has more IR-active phonon modes which contribute to a larger emissivity in the transparent portion of the atmosphere. Al_2O_3 has an even higher band gap than $BaSO_4$, which does not offer further benefits but decreases the refractive index. In the sky window, on the other hand, we find that although the κ peaks of $BaSO_4$ are lower than α-SiO_2 in the 8−13 μm band, they are much broader and produce a more uniformly high κ profile. This is partly due to the fact that $BaSO_4$ owns more IR-active optical phonon modes than that of α-SiO_2 in the sky window, but further, the effect of 4ph scattering on the phonon damping is non-negligible for α-SiO_2 and even stronger in $BaSO_4$ at room temperature, as shown in Fig. 3(b)-3(c). Therefore, both 3ph and 4ph scattering should be considered. As seen in Fig. 3(c), 4ph scattering lowers the κ peak magnitudes but significantly broaden the peaks, providing a previously unknown favorable mechanism for more uniformly high absorption. In addition, we show that using phenomenological phonon linewidths does not yield satisfactory results (Supplemental Material, Fig. S2).

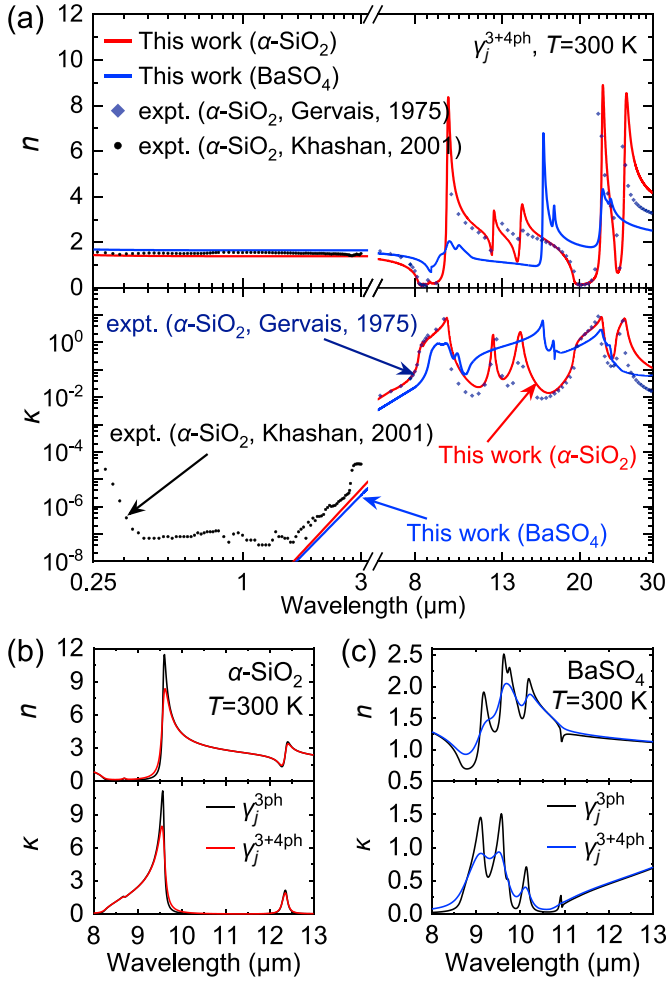

Fig. 3. (a) n and κ of α-SiO_2 and $BaSO_4$. The experimental data of α-SiO_2 in both solar spectrum [71] (black circle dot) and mid-IR region [70] (navy diamond dot) are plotted for comparison. n and κ of α-SiO_2 in (b) and $BaSO_4$ in (c) in the sky window region (8−13 μm), respectively, by considering only 3ph scattering and both 3ph and 4ph scattering (3+4ph) at room temperature.

3.3. Reflectance/emittance of nanocomposites from Monte Carlo

Next we investigate the radiative cooling performance in nanocomposite systems where the micro/nano-particulates are embedded in polymer. The Mie-theory [32,50,75] is employed to obtain the scattering properties of single particles and further a particle bed with size distribution. The properties are given in Supplemental Material, Fig. S3. Monte Carlo simulations are then performed to obtain the emittance, reflectance, and transmittance of nanocomposites consisting of $BaSO_4$ (or SiO_2) nanoparticles in an acrylic matrix. It is worth mentioning that we use the above predicted n and κ from first-principles as the input parameters to conduct the Monte Carlo simulation without any fitting parameters, indicating that our approach can predict radiative cooling properties of materials for which optical constants are not available in the literature. It makes possible the high-throughput screening of a large number of materials to guide experimental efforts in the future. To be consistent with the materials parameters in experiments [34,36], here we present simulation results for $BaSO_4$-acrylic composite with volume fraction of 60%, particle diameter of 398.4 ± 130 nm, and thickness of 400 μm, as shown in Fig. 4(a). The results are compared to experimental data in the figure, and the overall agreement demonstrates the accuracy of our predictive approach based on first-principles calculations and Monte Carlo simulations. It should be noted that the not exactly well-matched reflectance/emittance specially in the near-infrared (NIR) region is mainly attributed to neglecting the effects of the absorbing polymer matrix in the Monte Carlo simulation. This is because the calculations use the Lorentz-Mie theory to calculate the spectral scattering and absorption coefficients, and the Lorentz-Mie theory does not account for participating media, i.e. matrix absorption. The polymer matrix absorptance in the NIR cause the oscillations in the experimental data that the Monte Carlo simulations do not capture. This has been explicitly demonstrated in our previous work [32]. Importantly, the total solar reflectance is 95.7% for $BaSO_4$ and higher than 91.8% for α-SiO_2, and this is due to the higher refractive index of $BaSO_4$. We note that the total solar reflectance is underpredicted (97.5%) as compared to the experimental measurement (98.1% [36]). The reason why Monte Carlo underpredicts the total

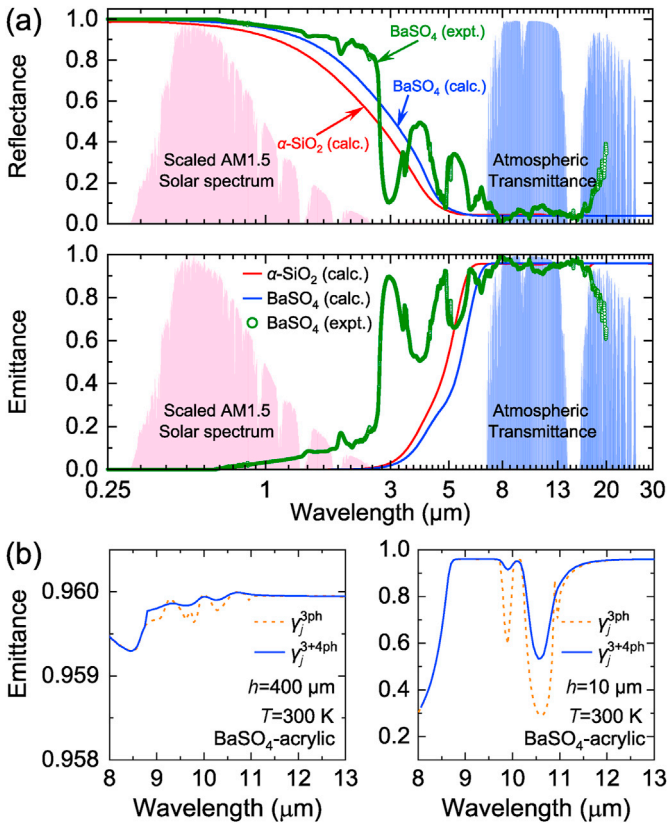

Fig. 4. (a) Predicted reflectance and emittance of α-SiO_2-acrylic (red line) and $BaSO_4$-acrylic (blue line) nanocomposites from Monte Carlo simulation with particle diameter of 398.4 ± 130 nm, volume fraction of 60%, and film thickness of 400 μm. The $BaSO_4$ results are compared to available experimental data [34,36]. The scaled AM1.5 solar spectrum [73] (red area) and the clear sky atmospheric transmittance in the mid-infrared region [74] (blue area) are plotted for reference. (b) Spectral-emittance by considering 3ph (dashed line) and 3+4ph (solid line) scatterings in $BaSO_4$-acrylic nanocomposites with different film thickness h.

solar reflectance is that the experimentally measured film is a porous media with air voids in the acrylic-$BaSO_4$ nanocomposites. The air voids create more specular scattering due to the larger refractive index contrast from the air to the matrix or the air to the $BaSO_4$, when compared to the matrix to $BaSO_4$ refractive index contrast. Our Monte Carlo simulations assume a uniform dispersion of $BaSO_4$ in a pure acrylic matrix, no air voids, which creates less specular scattering leading to an underpredicted reflectance. In the sky window, the total absorptance or emittance of $BaSO_4$-acrylic nanocomposite is 0.96, which agrees with experimental data, and is overall larger than the predicted value 0.94 of α-SiO_2. This can be attributed to the more uniformly higher κ in $BaSO_4$ in the sky window than in α-SiO_2. The results of thickness-dependent emittance in the wavelength range of 0.25−30 μm are provided in Supplemental Material, Fig. S4. We further highlight the phonon linewidth effects originated from 3ph to 3+4ph scattering on the sky window emittance at different coating thickness (h), as shown in Fig. 4(b) as well as Supplemental Material, Fig. S5. Although 4ph scattering makes a negligible impact on the sky window total emittance of 400 μm coating film because the film is thick enough to offset any low spectral κ value, it can enhance the total emittance by ~ 6% compared to 3ph only when h decreases to 10 μm shown in Fig. S5(b). The impact on the spectral emittance is even more evident at certain wavelengths in Fig. 4(b). Such enhancement, which comes from the 4ph scattering-induced broadening of the extinction index (κ) peaks, elucidates a previously unknown benefit of the 4ph scattering process. Future pursuit of radiative cooling will push to thiner coatings and other materials, and 4ph scattering should be considered in general. In addition, based on the theoretical cooling power calculations (see Fig. S6), the $BaSO_4$ maintains a consistent ~ 30 W/m^2 greater cooling power than SiO_2. The theoretical cooling power calculations further corroborate our hypothesis that $BaSO_4$ is a better candidate material than SiO_2 for radiative cooling applications.

4. Conclusions

We now summarize the comparison between $BaSO_4$ and α-SiO_2, which are both high-performance radiative cooling materials, to highlight why $BaSO_4$ is a more efficient radiative cooling pigment. First, although it is known that wide electronic band gap is needed to eliminate solar absorption, here we show that the band gap of $BaSO_4$ is also moderate enough to enable reasonably high refractive index for strong scattering. In fact, since the upper bound of energy in the solar spectrum is 4.13 eV, we suspect better performance than $BaSO_4$ is possible in materials with a band gap higher than 4.13 eV but lower than that of $BaSO_4$. Second, $BaSO_4$ has complex crystal structure and appropriate bond strength that yield a high number of infrared-active zone-center optical phonon modes in the Reststrahlen bands, and these modes show strong four-phonon scattering which is a previously unknown mechanism that contributes to the high emissivity in the sky window. Identifying such metrics is imperative for screening efficient radiative cooling materials. Moreover, we have demonstrated a multiscale simulation strategy combining first-principles calculation and Monte Carlo simulation to predict the radiative cooling properties of nanocomposites. When coupled with high-throughput search methods, our approach can efficiently identify the best radiative cooling materials among the large number of candidates in the future. The approach and insights may benefit other radiative applications as well, such as thermal barrier coatings (which also aims at high reflectance), concentrated solar receiver materials, thermophotovoltaic coatings, and variable emissivity coatings for space vehicles.

Author contributions

X.R., Z.T. and J.P. conceived and designed the research. X.R. and H.B. supervised the research. Z.T. performed the DFT calculations and J.P. performed the Monte Carlo calculations. Z.T. analyzed the data, prepared the figures and manuscript, with assistance and discussions from J.P., X.L., and X.Y. H.B. and X.R. revised the paper. Z.T. and J.P. contributed equally to this work. All authors discussed the results and contributed in writing the paper.

Declaration of competing interest

The authors declare that they have no known competing financial interests or personal relationships that could have appeared to influence the work reported in this paper.

Acknowledgment

Simulations were preformed at the Rosen Center for Advanced Computing (RCAC) of Purdue University. J.P., X.L., and X.R. thank the Cooling Technologies Research Center (CTRC) at Purdue University for partial support of this work. H.B. acknowledges the support by National Natural Science Foundation of China (Grant No. 51676121). Z.T. acknowledges the support of Chinese Scholarship Council (CSC, No. 201806230169), National Natural Science Foundation of China (Grant No. 52106068), China Postdoctoral Science Foundation (Grant No. 2020M680127), Guangdong Basic and Applied Basic

Research Foundation (Grants No. 2020A1515110838 and No. 2021A1515011688), and Shenzhen Science and Technology Program (Grant No. RCBS20200714114919142).

Appendix A. Supplementary data

Supplementary data to this article can be found online at https://doi.org/10.1016/j.mtphys.2022.100658.

References

[1] D. Michell, K. Biggs, Radiation cooling of buildings at night, Appl. Energy 5 (4) (1979) 263–275, https://doi.org/10.1016/0306-2619(79)90017-5. https://linkinghub.elsevier.com/retrieve/pii/0306261979900175.

[2] L. Zhu, A. Raman, K.X. Wang, M.A. Anoma, S. Fan, Radiative cooling of solar cells, Optica 1 (1) (2014) 32, https://doi.org/10.1364/OPTICA.1.000032. https://www.osapublishing.org/abstract.cfm?URI=optica-1-1-32.

[3] M. Zeyghami, F. Khalili, Performance improvement of dry cooled advanced concentrating solar power plants using daytime radiative cooling, Energy Convers. Manag. 106 (2015) 10–20, https://doi.org/10.1016/j.enconman.2015.09.016. http://www.sciencedirect.com/science/article/pii/S0196890415008511.

[4] C. Liu, J. Fan, H. Bao, Hydrophilic radiative cooler for direct water condensation in humid weather, Sol. Energ. Mat. Sol. C 216 (2020) 110700, https://doi.org/10.1016/j.solmat.2020.110700. http://www.sciencedirect.com/science/article/pii/S0927024820302993.

[5] J. Xu, J. Zhang, B. Fu, C. Song, W. Shang, P. Tao, T. Deng, All-day freshwater harvesting through combined solar-driven interfacial desalination and passive radiative cooling, ACS Appl. Mater. Interfaces 12 (2020) 47612–47622. https://pubs.acs.org/doi/abs/10.1021/acsami.0c14773.

[6] R. Family, M.P. Mengüç, Materials for radiative cooling: a review, Procedia Environ. Sci. 38 (2017) 752–759, https://doi.org/10.1016/j.proenv.2017.03.158. http://www.sciencedirect.com/science/article/pii/S187802961730169X.

[7] X. Sun, Y. Sun, Z. Zhou, M.A. Alam, P. Bermel, Radiative sky cooling: fundamental physics, materials, structures, and applications, Nanophotonics 6 (5) (2017) 997–1015, https://doi.org/10.1515/nanoph-2017-0020. http://www.degruyter.com/view/j/nanoph.2017.6.issue-5/nanoph-2017-0020/nanoph-2017-0020.xml.

[8] M. Zeyghami, D.Y. Goswami, E. Stefanakos, A review of clear sky radiative cooling developments and applications in renewable power systems and passive building cooling, Sol. Energ. Mat. Sol. C 178 (2018) 115–128, https://doi.org/10.1016/j.solmat.2018.01.015. http://www.sciencedirect.com/science/article/pii/S092702481830014X.

[9] D. Zhao, A. Aili, Y. Zhai, S. Xu, G. Tan, X. Yin, R. Yang, Radiative sky cooling: fundamental principles, materials, and applications, Appl. Phys. Rev. 6 (2) (2019): 021306, https://doi.org/10.1063/1.5087281. http://aip.scitation.org/doi/10.1063/1.5087281.

[10] S. Catalanotti, V. Cuomo, G. Piro, D. Ruggi, V. Silvestrini, G. Troise, The radiative cooling of selective surfaces, Sol. Energy 17 (2) (1975) 83–89, https://doi.org/10.1016/0038-092X(75)90062-6. https://linkinghub.elsevier.com/retrieve/pii/0038092X75900626.

[11] A. Harrison, M. Walton, Radiative cooling of TiO_2 white paint, Sol. Energy 20 (2) (1978) 185–188, https://doi.org/10.1016/0038-092X(78)90195-0. https://linkinghub.elsevier.com/retrieve/pii/0038092X78901950.

[12] B. Orel, M.K. Gunde, A. Krainer, Radiative cooling efficiency of white pigmented paints, Sol. Energy 50 (6) (1993) 477–482, https://doi.org/10.1016/0038-092X(93)90108-Z. http://www.sciencedirect.com/science/article/pii/0038092X9390108Z.

[13] J. Pockett, Heat reflecting paints and a review of their advertising material, in: Chemeca 2010: Engineering at the Edge; 26-29 September 2010, Hilton Adelaide, South Australia, Hilton Adelaide, South Australia, Engineers Australia, 2010, p. 2999. https://search.informit.com.au/documentSummary;dn=995653800330276;res=IELENG.

[14] M.G. Meir, J.B. Rekstad, O.M. LØvvik, A study of a polymer-based radiative cooling system, Sol. Energy 73 (6) (2002) 403–417, https://doi.org/10.1016/S0038-092X(03)00019-7. http://www.sciencedirect.com/science/article/pii/S0038092X03000197.

[15] P. Grenier, Réfrigération radiative. Effet de serre inverse, Rev. Phys. Appl. 14 (1979) 87–90. https://rphysap.journaldephysique.org/en/articles/rphysap/abs/1979/01/rphysap_1979__14_1_87_0/rphysap_1979__14_1_87_0.html.

[16] A.R. Gentle, G.B. Smith, Radiative heat pumping from the earth using surface phonon resonant nanoparticles, Nano Lett 10 (2) (2010) 373–379, https://doi.org/10.1021/nl903271d. https://pubs.acs.org/doi/10.1021/nl903271d.

[17] B. Kimball, Cooling performance and efficiency of night sky radiators, Sol. Energy 34 (1) (1985) 19–33, https://doi.org/10.1016/0038-092X(85)90089-1. https://linkinghub.elsevier.com/retrieve/pii/0038092X85900891.

[18] A.F.G. Jacobs, B.G. Heusinkveld, S.M. Berkowicz, Passive dew collection in a grassland area, The Netherlands, Atmos. Res. 87 (3) (2008) 377–385, https://doi.org/10.1016/j.atmosres.2007.06.007. http://www.sciencedirect.com/science/article/pii/S0169809507001950.

[19] Z. Chen, L. Zhu, A. Raman, S. Fan, Radiative cooling to deep sub-freezing temperatures through a 24-h day–night cycle, Nat. Commun. 7 (1) (2016) 13729, https://doi.org/10.1038/ncomms13729. http://www.nature.com/articles/ncomms13729.

[20] J. Peoples, Y.-W. Hung, X. Li, D. Gallagher, N. Fruehe, M. Pottschmidt, C. Breseman, C. Adams, A. Yuksel, J. Braun, W.T. Horton, X. Ruan, Concentrated radiative cooling, Appl. Energy 310 (2022) 118368, https://doi.org/10.1016/j.apenergy.2021.118368. https://linkinghub.elsevier.com/retrieve/pii/S0306261921016111.

[21] A.P. Raman, M.A. Anoma, L. Zhu, E. Rephaeli, S. Fan, Passive radiative cooling below ambient air temperature under direct sunlight, Nature 515 (7528) (2014) 540–544, https://doi.org/10.1038/nature13883. https://www.nature.com/articles/nature13883.

[22] A.R. Gentle, G.B. Smith, A subambient open roof surface under the mid-summer sun, Adv. Sci. 2 (9) (2015) 1500119, https://doi.org/10.1002/advs.201500119. https://onlinelibrary.wiley.com/doi/abs/10.1002/advs.201500119.

[23] Y. Zhai, Y. Ma, S.N. David, D. Zhao, R. Lou, G. Tan, R. Yang, X. Yin, Scalable-manufactured randomized glass-polymer hybrid metamaterial for daytime radiative cooling, Science 355 (6329) (2017) 1062–1066, https://doi.org/10.1126/science.aai7899. https://www.sciencemag.org/lookup/doi/10.1126/science.aai7899.

[24] J.-l. Kou, Z. Jurado, Z. Chen, S. Fan, A.J. Minnich, Daytime radiative cooling using near-black infrared emitters, ACS Photonics 4 (3) (2017) 626–630, https://doi.org/10.1021/acsphotonics.6b00991. https://pubs.acs.org/doi/10.1021/acsphotonics.6b00991.

[25] B. Ko, D. Lee, T. Badloe, J. Rho, Metamaterial-based radiative cooling: towards energy-free all-day cooling, Energies 12 (1) (2018) 89, https://doi.org/10.3390/en12010089. http://www.mdpi.com/1996-1073/12/1/89.

[26] M. Kim, D. Lee, S. Son, Y. Yang, H. Lee, J. Rho, Visibly transparent radiative cooler under direct sunlight, Adv. Opt. Mater. 9 (13) (2021) 2002226, https://doi.org/10.1002/adom.202002226. https://onlinelibrary.wiley.com/doi/10.1002/adom.202002226.

[27] D. Chae, H. Lim, S. So, S. Son, S. Ju, W. Kim, J. Rho, H. Lee, Spectrally selective nanoparticle mixture coating for passive daytime radiative cooling, ACS Appl. Mater. Interfaces 13 (18) (2021) 21119–21126, https://doi.org/10.1021/acsami.0c20311. https://pubs.acs.org/doi/10.1021/acsami.0c20311.

[28] D. Lee, M. Go, S. Son, M. Kim, T. Badloe, H. Lee, J.K. Kim, J. Rho, Sub-ambient daytime radiative cooling by silica-coated porous anodic aluminum oxide, Nano Energy 79 (2021) 105426, https://doi.org/10.1016/j.nanoen.2020.105426. https://linkinghub.elsevier.com/retrieve/pii/S2211285520310028.

[29] T. Li, Y. Zhai, S. He, W. Gan, Z. Wei, M. Heidarinejad, D. Dalgo, R. Mi, X. Zhao, J. Song, J. Dai, C. Chen, A. Aili, A. Vellore, A. Martini, R. Yang, J. Srebric, X. Yin, L. Hu, A radiative cooling structural material, Science 364 (6442) (2019) 760–763, https://doi.org/10.1126/science.aau9101. https://www.sciencemag.org/lookup/doi/10.1126/science.aau9101.

[30] Z. Huang, X. Ruan, Nanoparticle embedded double-layer coating for daytime radiative cooling, Int. J. Heat Mass Tran. 104 (2017) 890–896. https://www.sciencedirect.com/science/article/pii/S0017931016309255.

[31] H. Bao, C. Yan, B. Wang, X. Fang, C.Y. Zhao, X. Ruan, Double-layer nanoparticle-based coatings for efficient terrestrial radiative cooling, Sol. Energ. Mat. Sol. C 168 (2017) 78–84, https://doi.org/10.1016/j.solmat.2017.04.020. http://www.sciencedirect.com/science/article/pii/S0927024817301836.

[32] J. Peoples, X. Li, Y. Lv, J. Qiu, Z. Huang, X. Ruan, A strategy of hierarchical particle sizes in nanoparticle composite for enhancing solar reflection, Int. J. Heat Mass Tran. 131 (2019) 487–494, https://doi.org/10.1016/j.ijheatmasstransfer.2018.11.059. http://www.sciencedirect.com/science/article/pii/S0017931018334665.

[33] J. Mandal, Y. Fu, A.C. Overvig, M. Jia, K. Sun, N.N. Shi, H. Zhou, X. Xiao, N. Yu, Y. Yang, Hierarchically porous polymer coatings for highly efficient passive daytime radiative cooling, Science 362 (6412) (2018) 315–319, https://doi.org/10.1126/science.aat9513. https://www.sciencemag.org/lookup/doi/10.1126/science.aat9513.

[34] X. Ruan, X. Li, Z. Huang, J.A. Peoples, WO2020072818 - metal-free solar-reflective infrared-emissive paints and methods of producing the same, Patent application no. PCT/US2019/054566, filed October 3, 2019, and published (Apr.), https://patents.google.com/patent/WO2020072818A1/en, April 9, 2020.

[35] X. Li, J. Peoples, Z. Huang, Z. Zhao, J. Qiu, X. Ruan, Full daytime sub-ambient radiative cooling in commercial-like paints with high figure of merit, Cell Rep. Physical Science 1 (10) (2020) 100221, https://doi.org/10.1016/j.xcrp.2020.100221. https://linkinghub.elsevier.com/retrieve/pii/S2666386420302368.

[36] X. Li, J. Peoples, P. Yao, X. Ruan, Ultrawhite $BaSO_4$ paints and films for remarkable daytime subambient radiative cooling, ACS Appl. Mater. Interfaces 13 (18) (2021) 21733–21739, https://doi.org/10.1021/acsami.1c02368. https://pubs.acs.org/doi/10.1021/acsami.1c02368.

[37] M. Rohlfing, S.G. Louie, Electron-hole excitations in semiconductors and insulators, Phys. Rev. Lett. 81 (11) (1998) 2312–2315, https://doi.org/10.1103/PhysRevLett.81.2312. https://link.aps.org/doi/10.1103/PhysRevLett.81.2312.

[38] S. Albrecht, L. Reining, R. Del Sole, G. Onida, *Ab initio* calculation of excitonic effects in the optical spectra of semiconductors, Phys. Rev. Lett. 80 (20) (1998) 4510–4513, https://doi.org/10.1103/PhysRevLett.80.4510. https://link.aps.org/doi/10.1103/PhysRevLett.80.4510.

[39] E.K. Chang, M. Rohlfing, S.G. Louie, Excitons and optical properties of α-quartz, Phys. Rev. Lett. 85 (12) (2000) 2613–2616. https://journals.aps.org/prl/abstract/10.1103/PhysRevLett.85.2613.

[40] H. Bao, X. Ruan, Ab initio calculations of thermal radiative properties: the semiconductor GaAs, Int. J. Heat Mass Tran. 53 (7–8) (2010) 1308–1312, https://doi.org/10.1016/j.ijheatmasstransfer.2009.12.033. https://linkinghub.elsevier.com/retrieve/pii/S0017931009006930.

[41] G. Kresse, M. Marsman, L.E. Hintzsche, E. Flage-Larsen, Optical and electronic properties of Si_3N_4 and α-SiO_2, Phys. Rev. B 85 (4) (2012): 045205, https://doi.org/10.1103/PhysRevB.85.045205. https://link.aps.org/doi/10.1103/PhysRevB.85.045205.

[42] J.Y. Yang, L.H. Liu, J.Y. Tan, Temperature-dependent dielectric function of germanium in the uv-vis spectral range: a first-principles study, J. Quant. Spectrosc. Radiat. Transf. 141 (2014) 24–30, https://doi.org/10.1016/j.jqsrt.2014.02.026. http://www.sciencedirect.com/science/article/pii/S0022407314000831.

[43] Z. Tong, L. Liu, L. Li, H. Bao, Temperature-dependent infrared optical properties of 3C-, 4H- and 6H-SiC, Phys. B Condens. Matter 537 (2018) 194–201, https://doi.org/10.1016/j.physb.2018.02.023. http://www.sciencedirect.com/science/article/pii/S092145261830142X.

[44] Z. Tong, X. Yang, T. Feng, H. Bao, X. Ruan, First-principles predictions of temperature-dependent infrared dielectric function of polar materials by including four-phonon scattering and phonon frequency shift, Phys. Rev. B 101 (12) (2020) 125416, https://doi.org/10.1103/PhysRevB.101.125416. https://link.aps.org/doi/10.1103/PhysRevB.101.125416.

[45] X. Yang, T. Feng, J.S. Kang, Y. Hu, J. Li, X. Ruan, Observation of strong higher-order lattice anharmonicity in Raman and infrared spectra, Phys. Rev. B 101 (16) (2020) 161202, https://doi.org/10.1103/PhysRevB.101.161202. https://link.aps.org/doi/10.1103/PhysRevB.101.161202.

[46] Z. Tong, T. Dumitrică, T. Frauenheim, First-principles prediction of infrared phonon and dielectric function in biaxial hyperbolic van der Waals crystal a-MoO3, Phys. Chem. Chem. Phys. 23 (2021) 19627–19635, https://doi.org/10.1039/d1cp00682g.

[47] M.F. Modest, Radiative Heat Transfer, third ed., Academic Press, New York, 2013.

[48] J.R.M. Howell, M.P.S. Robert, Thermal Radiation Heat Transfer, sixth ed., CRC Press, Boca Raton, 2016.

[49] L. Wang, S.L. Jacques, Monte Carlo Modeling of Light Transport in Multi-Layered Tissues in Standard C, University of Texas M. D. Anderson Cancer Center, 1992, pp. 1–167. http://coilab.caltech.edu/mcr5/Mcman.pdf.

[50] S. Redmond, S.C. Rand, X.L. Ruan, M. Kaviany, Multiple scattering and nonlinear thermal emission of Yb^{3+}, Er^{3+}:Y_2O_3 nanopowders, J. Appl. Phys. 95 (8) (2004) 4069–4077, https://doi.org/10.1063/1.1667274. http://aip.scitation.org/doi/10.1063/1.1667274.

[51] Z.M. Zhang, Nano/microscale Heat Transfer, McGraw-Hill, New York, 2007.

[52] M. Gajdoš, K. Hummer, G. Kresse, J. Furthmüller, F. Bechstedt, Linear optical properties in the projector-augmented wave methodology, Phys. Rev. B 73 (4) (2006): 045112, https://doi.org/10.1103/PhysRevB.73.045112. https://link.aps.org/doi/10.1103/PhysRevB.73.045112.

[53] A.S. Barker, Transverse and longitudinal optic mode study in MgF_2 and ZnF_2, Phys. Rev. 136 (5A) (1964) A1290–A1295, https://doi.org/10.1103/PhysRev.136.A1290. https://link.aps.org/doi/10.1103/PhysRev.136.A1290.

[54] M. Schubert, Coordinate-invariant lyddane-sachs-teller relationship for polar vibrations in materials with monoclinic and triclinic crystal systems, Phys. Rev. Lett. 117 (21) (Nov. 2016). https://link.aps.org/doi/10.1103/PhysRevLett.117.215502.

[55] G. Kresse, D. Joubert, From ultrasoft pseudopotentials to the projector augmented-wave method, Phys. Rev. B 59 (3) (1999) 1758–1775, https://doi.org/10.1103/PhysRevB.59.1758. https://link.aps.org/doi/10.1103/PhysRevB.59.1758.

[56] G. Kresse, J. Hafner, *Ab initio* molecular dynamics for liquid metals, Phys. Rev. B 47 (1) (1993) 558–561, https://doi.org/10.1103/PhysRevB.47.558. https://link.aps.org/doi/10.1103/PhysRevB.47.558.

[57] A. Alkauskas, P. Broqvist, A. Pasquarello, Defect energy levels in density functional calculations: alignment and band gap problem, Phys. Rev. Lett. 101 (4) (2008): 046405, https://doi.org/10.1103/PhysRevLett.101.046405. https://link.aps.org/doi/10.1103/PhysRevLett.101.046405.

[58] A. Togo, I. Tanaka, First principles phonon calculations in materials science, Scripta Mater. 108 (2015) 1–5, https://doi.org/10.1016/j.scriptamat.2015.07.021. https://linkinghub.elsevier.com/retrieve/pii/S1359646215003127.

[59] W. Li, J. Carrete, N.A. Katcho, N. Mingo, ShengBTE: a solver of the Boltzmann transport equation for phonons, Comput. Phys. Commun. 185 (6) (2014) 1747–1758, https://doi.org/10.1016/j.cpc.2014.02.015. http://linkinghub.elsevier.com/retrieve/pii/S0010465514000484.

[60] T. Feng, X. Ruan, Quantum mechanical prediction of four-phonon scattering rates and reduced thermal conductivity of solids, Phys. Rev. B 93 (4) (2016): 045202, https://doi.org/10.1103/PhysRevB.93.045202. https://link.aps.org/doi/10.1103/PhysRevB.93.045202.

[61] Z. Tong, T. Dumitrică, T. Frauenheim, Ultralow thermal conductivity in two-dimensional MoO_3, Nano Lett 21 (10) (2021) 4351–4356, https://doi.org/10.1021/acs.nanolett.1c00935. https://pubs.acs.org/doi/10.1021/acs.nanolett.1c00935.

[62] Z. Han, X. Yang, W. Li, T. Feng, X. Ruan, FourPhonon: an extension module to ShengBTE for computing four-phonon scattering rates and thermal conductivity, Comput. Phys. Commun. 270 (2022) 108179, https://doi.org/10.1016/j.cpc.2021.108179. https://linkinghub.elsevier.com/retrieve/pii/S0010465521002915.

[63] Z. Tong, A. Pecchia, C. Yam, T. Dumitrică, T. Frauenheim, Significant increase of electron thermal conductivity in Dirac semimetal beryllonitrene by doping beyond van hove singularity, Adv. Funct. Mater. (2022) 2111556doi, https://doi.org/10.1002/adfm.202111556. https://onlinelibrary.wiley.com/doi/full/10.1002/adfm.202111556.

[64] doi:See Supplemental Material at [URL] for Computational Details on the Lattice Structure Optimization of α-SO_2 and $BaSO_4$, IFCs Computation, IR-Active Phonon Parameters, Monte Carlo Simulations, Scattering and Absorption Coefficients, and Radiative cooling power calculations.

[65] A.M. Amiryan, A.M. Gurvieh, R.V. Katomina, I.Y. Petrova, N.P. Soshchin, M.I. Tombak, Recombination processes and emission spectrum of terbium in oxysulfides, J. Appl. Spectrosc. 27 (3) (1977) 1159–1162, https://doi.org/10.1007/BF00625902.

[66] D. Strauch, B. Dorner, Lattice dynamics of alpha -quartz. I. Experiment, J. Phys. Condens. Matter 5 (34) (1993) 6149–6154, https://doi.org/10.1088/0953-8984/5/34/003.

[67] E. Kroumova, M. Aroyo, J. Perez-Mato, A. Kirov, C. Capillas, S. Ivantchev, H. Wondratschek, Bilbao crystallographic server : useful databases and tools for phase-transition studies, Phase Transitions 76 (1–2) (2003) 155–170, https://doi.org/10.1080/0141159031000076110. http://www.tandfonline.com/doi/abs/10.1080/0141159031000076110.

[68] A.M. Glazer, *Vibrate!* A program to compute irreducible representations for atomic vibrations in crystals, J. Appl. Crystallogr. 42 (6) (2009) 1194–1196, https://doi.org/10.1107/S0021889809040424. http://scripts.iucr.org/cgi-bin/paper?S0021889809040424.

[69] H.R. Philipp, Optical transitions in crystalline and fused quartz, Solid State Commun 4 (1) (1966) 73–75, https://doi.org/10.1016/0038-1098(66)90109-8. http://www.sciencedirect.com/science/article/pii/0038109866901098.

[70] F. Gervais, B. Piriou, Temperature dependence of transverse and longitudinal optic modes in the α and β phases of quartz, Phys. Rev. B 11 (10) (1975) 3944–3950, https://doi.org/10.1103/PhysRevB.11.3944. https://link.aps.org/doi/10.1103/PhysRevB.11.3944.

[71] M.A. Khashan, A.Y. Nassif, Dispersion of the optical constants of quartz and polymethyl methacrylate glasses in a wide spectral range: 0.2–3 μm, Opt Commun. 188 (1) (2001) 129–139, https://doi.org/10.1016/S0030-4018(00)01152-4. http://www.sciencedirect.com/science/article/pii/S0030401800011524.

[72] N. Ravindra, P. Ganapathy, J. Choi, Energy gap–refractive index relations in semiconductors - an overview, Infrared Phys. Technol. 50 (1) (2007) 21–29, https://doi.org/10.1016/j.infrared.2006.04.001. https://linkinghub.elsevier.com/retrieve/pii/S135044950600048X.

[73] ASTM G159-98, Standard Tables for References Solar Spectral Irradiance at Air Mass 1.5: Direct Normal and Hemispherical for a 37° Tilted Surface (Withdrawn 2005), Tech. rep., ASTM International, 1998 http://www.astm.org/cgi-bin/resolver.cgi?G159-98.

[74] S.D. Lord, A new software tool for computing Earth's atmospheric transmission of near- and far-infrared radiation, Tech. rep. https://ntrs.nasa.gov/search.jsp?R=19930010877, Dec. 1992.

[75] C.F. Bohren, D.R. Huffman, Absorption and Scattering of Light by Small Particles, Wiley, New York, 1983.